Visualizing Model Data Using A Fast Approximation of a Radiative Transfer Model

Valliappa Lakshmanan[1,2]*, Robert Rabin[2], Jason Otkin[3],

John S. Kain[2], Scott Dembek[1,2]

*Corresponding author: V Lakshmanan, 120 David L. Boren Blvd, Norman OK 73072; lakshman@ou.edu

[1]Cooperative Institutute of Mesoscale Meteorological Studies, University of Oklahoma; [2]National Oceanic and Atmospheric Administration / National Severe Storms Laboratory; [3]Space Science and Engineering Center, Univ. Wisconsin, Madison

ABSTRACT

Visualizing model forecasts using simulated satellite imagery have proven very useful because cloud imagery can provide inferences about physical processes not associated with precipitation. A forward radiative transfer model is capable of providing such a visible channel depiction of numerical weather prediction model output, but present-day forward models are too slow to run routinely on operational model forecasts.

It is demonstrated that it is possible to approximate the radiative transfer model using an universal approximator whose parameters can be determined by fitting the output of the forward model to inputs derived from the model forecasts from which it was computed. The resulting approximation is very close to the complex radiative transfer model and has the advantage that it can be computed in a matter of minutes. This approximation is carried out on model forecasts to demonstrate its utility as a visualization and forecasting tool.

1. Introduction

Precipitation forecasts from numerical weather prediction (NWP) models have traditionally been presented to forecasters as accumulated depth over specified time intervals, say, 6 hours. Guidance regarding clouds has generally been lacking, aside from post-processed statistics about general cloud properties such as cloud cover (e.g. Jakob (1999); Teixeira and Hogan (2002)). Part of the reason for this rather ambiguous presentation of clouds and precipitation is that many aspects of these features have been parameterized in forecast models, rather than explicitly represented on the model grid (e.g. Sundqvist et al. (1989); Janjic (1990)). However, in recent years increases in computer power have allowed opera-

tional NWP centers to increase spatial resolution and explicitly resolve more key processes, such as deep precipitating convection, that were previously parameterized (e.g. Weiss et al. (2008); Dixon et al. (2009)). This transition has allowed for the development of new ways to visualize explicit forecasts for clouds and precipitation.

Most of this visualization work has focused on precipitation. Explicit precipitation output predicted by NWP models with grid spacing on the order of several km is now commonly viewed as a simulated reflectivity product (e.g., Kain et al. (2008)). This product is particularly revealing not so much because it depicts the instantaneous precipitation rate, but because the patterns formed by simulated reflectivity fields can be used to infer a multitude of circulations, processes, and configurations associated with precipitating weather systems (Koch et al. 2005). Simulated reflectivity provides useful guidance for forecasters (e.g., Weisman et al. (2008)) and has been used for model validation in numerous arenas, such as the National Oceanic and Atmospheric Administration Hazardous Weather Testbed (NOAA HWT) (e.g. Kain et al. (2010b)).

Visualization of clouds, in the form of simulated satellite imagery, can also provide unique information about NWP model output (e.g., Otkin and Greenwald (2008); Otkin et al. (2009)). Although synthetic satellite imagery has received less attention in the weather forecasting community, it may ultimately prove to be more valuable than simulated reflectivity because most clouds are non-precipitating. Thus cloud imagery can provide inferences about physical processes not associated with precipitation (e.g., Feltz et al. (2009)) and/or processes that could allow forecasters to anticipate better the development of precipitation. Synthetic satellite imagery has also proven to be useful in the NOAA HWT in recent years (Clark et al. 2011).

One way to calculate the reflectance for the GOES $0.65\mu m$ channel is to use a complex forward modeling system such as the Successive Order of Interaction (SOI) model developed by Heidinger et al. (2006) wherein gas optical depths are computed for each model layer and absorption and scattering properties are applied to each hydrometeor species predicted by the model microphysics parameterization scheme.

Even with the recent development of fast forward radiative transfer models, computing simulated satellite observations, particularly those for visible channels, remains a very time consuming task. For instance, approximately 13 hours are required to compute GOES $0.65\mu m$ reflectances for a single time step on the NSSL-WRF operational model domain (750 x 980 grid points) using the SOI model. Though the wall clock time could be substantially reduced by using multiple processors, the overall high computational cost remains and renders the real time generation of such observations difficult using present computational resources. Because of this, it is useful to explore other means to generate simulated visible satellite imagery in real time. In this paper, we suggest the approach of creating an approximation of the forward model using a parametric approximation.

Neural networks (NNs) are a non-linear statistical modeling tool that were motivated by analogies to biological neural networks. Neural networks have enjoyed widespread use in meteorological applications, ranging from prediction of rainfall amounts (Venkatesan et al. 1997), and diagnosing tornado probability (Marzban and Stumpf 1996) to quality control (Lakshmanan et al. 2007). However, all these uses of neural networks are data-driven, aiming to predict a desired value based on inputs whose individual impacts are unknown. Our use of neural networks is as an approximating mechanism, to approximate a known function that is too complex to compute. In other words, we know the exact impact of each

input variable, but the transfer functions are too time-consuming to compute. The use of a neural network as a functional approximation is rarer in meteorological applications, but has been explored before, notably by Krasnopolsky et al. (2008).

We employed a neural network of the form:

$$y = \sum_{j=1}^{M} w_j h(\sum_{i=0}^{d} w_{ji} x_i) \tag{1}$$

where y is the output of the NN and the x_is are the inputs (there are d "true" inputs with x_0 fixed to be a constant value of 1). The ws are referred to as the weights and the "transfer function" $h(x)$ is given by:

$$h(x) = \frac{1}{1 + e^{-x}} \tag{2}$$

Each layer of transfer functions in the neural network adds a "hidden layer" i.e. a set of transformations whose inputs and outputs are not the inputs and output of the equation as a whole. In this case, the input of the hidden layer is a weighted combination of the input values x_i. The output y of the NN is a weighted combination of the results of the transfer function at each of the M hidden nodes. Neural networks of this form are capable of approximating any continuous functional mapping to arbitrary accuracy and are therefore suitable for use as universal approximators (Bishop 1995).

A natural question that arises is why we need to approximate the forward model using the NN, rather than have the NN approximate the observed visible field directly. There are several problems with training a NN to estimate visible channel reflectance from model fields, but the key problem is that model forecasts (and even analysis fields) suffer from displacement and distortion errors. In addition, some clouds visible on satellite imagery may not be depicted in the model and vice-versa. Finally, the satellite visible imagery is

influenced by surface reflectance, darkening due to sun angle, parallax errors, shadows, etc. all of which would have to be accounted for when training a NN to predict the observed value. Using a forward model where some of these effects can be switched off provides more control when training a NN.

2. Approximating the Forward Model

The radiative transfer forward model was run on a representative set of numerical model data. At each 2D pixel of the model grid, data values from various model fields (mixing ratios, temperature, pressure, etc.) were used as inputs to a neural network. The goal of training was for the resulting neural network to yield the best possible approximation of what the forward model does on the dataset.

a. Training dataset

The optimization (or "training") process for the NN consists of finding the best set of w's that will allow the output of the neural network to approximate the behavior of the radiative transfer forward model on the dataset. In other words, the target value, y_t, is obtained from the radiative transfer model and the input x_is are obtained from the NWP model forecast. The NN training process consists of determining the weights, ws, at which the square error computed over all the pixels of the training dataset (i.e. $\sum(y_t - y)^2$) is minimum.

The input dataset consisted of outputs from a Weather Research and Forecasting (WRF: Skamarock et al. (2005)) model that is run routinely at the National Severe Storms Laboratory

(NSSL), hereafter, the NSSL-WRF (Kain et al. 2010a). The NSSL-WRF has a 4 km grid length (grid size of 1200x800), 35 vertical levels and a time step of 24 seconds. It uses the WRF single-moment 6-Class microphysics scheme (WSM6) microphysics scheme of Hong and Lim (2006). Initial and laternal boundary conditions are obtained from the North American Model (Rogers et al. 2009).

The input dataset consisted of NSSL-WRF model forecasts for 18Z to 23Z in one-hour increments on Apr. 3, 1974, July 1, 2009, Aug 12-16 2009 excluding Aug. 15, 2009. At that time, the NSSL-WRF domain was 980x750, covering the eastern 2/3rds of the continental United States. These model forecasts were provided to the forward model and the resulting visible channel reflectance values stored for each grid point at each time period. Because these datasets cover a wide area, this dataset captures a wide variety of weather situations.

One problem is that even with just six days of data, the representative training sets are incredibly large. We used data from 36 forecasts in order to train the model. Thus, the size of the input is about 26.5 million patterns (there is one pattern corresponding to every NSSL-WRF surface grid point). The model fields are numerous as well. Fourteen 3D fields such as temperature and perturbation geopotential are produced at every time step and for each of these fields, one would have to consider 35 vertical slices. In addition, there are 67 2D fields such as precipitation and soil moisture. Using all of the possible inputs would result in a training set that is about 15 billion points, a rather unrealistic option. Hence, we reduced the number of inputs by vertically integrating some of the 3D fields and choosing the input parameters based on the variables considered by the radiative transfer model and how these variables were employed within it.

In the forward model of Heidinger et al. (2006), gas optical depths are computed for each

NSSL-WRF model layer using a lookup table containing layer atmospheric transmittances computed using line-by-line calculations. Ice cloud absorption and scattering properties, such as extinction efficiency, single scatter albedo, and full scattering phase function, obtained from the work of Baum et al. (2006) are subsequently applied to each frozen (i.e. cloud ice, snow, and graupel) hydrometeor species predicted by the WRF model microphysics parameterization scheme. A lookup table based on Lorenz-Mie calculations (for the scattering of electromagnetic radiation) is used to assign the properties for the liquid (cloud water and rain water) species. Visible cloud optical depths are calculated separately for the liquid and frozen hydrometeor species following the work of Han et al. (1995) and Heymsfield et al. (2003), respectively. Surface albedo and emissivity are obtained for land grid points using the Filled Land Surface Albedo Product dataset developed by the MODIS atmospheric science team[1]. Over water surfaces, changes in reflectance due to waves and sun glint are considered using the model developed by Sayer et al. (2010). Finally, the simulated skin temperature and atmospheric temperature profiles along with the layer gas optical depths and cloud scattering properties are input into the Successive Order of Interaction (SOI) forward radiative transfer model (Heidinger et al. 2006), which is used to compute the simulated visible reflectances.

The neural network is expected to approximate all these computations by the universal approximator shown in Equation 1, except for the following modifications. Usually, the forward model takes the sun angle into account in order to darken the visible image appropriately. Since our goal is to create a synthetic visible field for the purpose of visualizing the model microphysics, darkening the image is inappropriate – there is no reason why one

[1]http://modis-atmos.gsfc.nasa.gov/ALBEDO/index.html

should not be able to visualize the model at night! Therefore, the forward model was modified to produce images with a fixed sun angle corresponding to local noon at all model output times. Another change that was made to the output of the forward model was to subtract out the surface albedo because a forecaster is interested in visualizing the cloud albedo and there is no need, in a synthetic field, to contaminate it with reflectance from the earth's surface.

Finally, all clear grid points (i.e. pixels where the mixing ratios of cloud water, cloud ice and snow were all zero) were removed from the training set as, according to the numerical model, there would be no cloudcover whatsoever at that point. In the output of the neural network when run on operational NSSL-WRF model forecasts, such points were assigned a visible reflectance value of zero.

From the NSSL-WRF model layers, the following variables were used to train the approximation to the forward model:

i. qvapor, qcloud, qrain, qice, qsnow, qgraup which are the mixing ratios (kg/kg) of water vapor, cloud water, rain, cloud ice, snow and graup respectively. These quantities which are available at every model layer were vertically integrated by weighting each layer's value with the thickness of that model layer in meters.

ii. qvapor, qcloud, qrain, qice, qsnow, qgraup (as above, but using only the top 17 model layers for the vertical integration.)

iii. qvapor, qcloud, qrain, qice, qsnow, qgraup (vertically integrated by weighting each layer's value by $presssure/temperature$ instead of by the thickness of the layer)

iv. minimum temperature, height of minimum temperature

v. Skin surface temperature (TSK)

vi. windspeed

b. Histogram equalization and downsampling

For the NSSL-WRF output on just these six days, there were a total of nearly 5 million grid points for which one of qcloud, qice and qsnow was non-zero. A histogram of the visible reflectance values (Figure 1) indicated that the majority of these values were low values. These aspects of the training dataset pose two problems: Firstly, training directly with the original dataset would cause a machine intelligence algorithm to focus on getting low visible reflectance values right at the expense of the far less frequent high reflectance values. This is, of course, unsuitable behavior. In order to use a visible field to visualize a model field, it is critical to get the higher visible reflectance values right – the low values are not quite as important. Secondly, five million data points is far too many for most machine intelligence or statistical software to handle on the type of computers (workstations with 4 GB of RAM) that we had on hand to do the training.

To address these issues, we carried out a process of histogram equalization and downsampling. We downsampled the nearly 5 million point dataset to a fifth of its size. These million grid points were obtained by randomly selecting grid points from the original dataset where the probability that a grid point was selected depended on its brightness value. Thus, grid points with a low brightness value had a lower probability of being selected while grid points with a high brightness value were more likely to be selected. The likelihood of a grid

point with brightness value b being selected depends on r, the repeat ratio, given by:

$$r = nS/P(b) \tag{3}$$

where n is the number of non-zero bins in the histogram, S the subsampling ratio (0.2 to reduce the dataset from 5 million points to 1 million) and $P(b)$ the probability density of that brightness value (read out from the histogram in Figure 1). If the r is, say 0.3, the grid point is selected with a probability of 0.3. This is achieved by generating a random number uniformly distributed in the range $[0 - 1]$ and selecting the point if the random number is below 0.3. If the r is 2.3, the grid point is selected twice and a third time with a probability of 0.3. To avoid overfitting extremely rare values, the repeat ratio was capped at 5.

After histogram equalization and subsampling, the resulting dataset of nearly million grid points had the frequency distribution shown in histogram on the right in Figure 1.

c. Neural network training

A neural network with 31 input variables and 3 hidden nodes (i.e. in Equation 1, $d = 31$ and $M = 3$) was trained on 1.01 million points selected through histogram equalization and randomized subsampling from a dataset consisting of 36 timesteps from 6 days of NSSL-WRF model runs. We experimented with increasing the number of hidden nodes (see Figure 2). While increasing the number of hidden nodes resulted in a lower mean square error in the approximation, this was subject to the classic bias-variance tradeoff. Thus, as shown in the second panel of Figure 2, using 9 hidden nodes would result in a larger bias but lower variance. We chose to use the neural network with 3 hidden nodes because it has the nice property of having nearly all errors bounded within 0.1 (the dotted horizontal lines) while having

only a slightly higher mean square error than the 9-node network (0.08 vs. 0.075). The approximation error ($y - y_t$) is is dimensionless and on the same scale as visible reflectance (0-1).

An example of the output of the forward model (run on NSSL-WRF model output valid at 20Z on Aug. 13, 2009) and the corresponding NN approximation are shown in Figure 3. Data from Aug. 13, 2009 were part of the training datasets. The bottom panels of Figure 3 show the output of the radiative transfer model and the NN approximation on NSSL-WRF forecast valid at 18Z on Aug. 28, 2009. This is a dataset that was not used in creating the approximation i.e. it was an independent test dataset. The first thing to note is that there are anticipated differences – the simulated imagery does not depict the land in areas where there is no cloudcover. Beyond that, the differences between the two images are only slight – some clouds appear brighter and others a little darker, but the cloud structure is faithfully represented in the approximation.

Magnitude differences between the output of the radiative transfer model and the NN approximation over the entire training dataset are shown in second panel of Figure 2. This analysis of errors was carried out over the original 5-million points in the training dataset i.e. before histogram equalization and downsampling. Looking at the graph for $M = 3$, it can be seen that the approximation errors are small and that the bias varies as a function of the "true" reflectance (i.e. reflectance value from the radiative transfer model). At very low values, below about 0.2, the approximation overestimates the reflectance (since the mean value of the approximation error,$y - y_t$, is greater than zero in this interval). At moderate values of reflectance, between about 0.2 and 0.5, the approximation tends to be an underestimate. At somewhat higher reflectance values, between about 0.5 and 0.7,

the approximation is again an overestimate – it is these clouds that appear brighter in the simulated imagery in Figure 3. Finally, the approximation underestimates extremely high values (reflectances above 0.7). We would like to caution that this graph should not be overanalyzed – the error magnitudes are almost all below 0.1 (shown by dotted horizontal lines). The error bars in the graph represent one standard deviation. Any biases that are present in the approximation are very small.

3. Visualization

The visible imagery are produced once a day at hourly intervals using input from the NSSL-WRF forecast microphysical data. Once the forecast has completed (approximately 4 hours from the initialization time, 00 UTC), the visible images are produced within 5 minutes on a single workstation. The full forward model, on the other hand, would have required a few hours computation time to run on a cluster of workstations.

Output of the visible imagery are made available for viewing on the web with options of two background fields: clear-sky surface albedo, and Normalized Difference Vegetation Index (NDVI).[2]

The surface albedo is provided by the radiative transfer forward model of (Heidinger et al. 2006) and is based on solar elevation angles from August 2009. The NDVI data are produced from a 14-day composite of NOAA/AVHRR data by the USGS EROS Data Center. The data currently used as the background for the visible imagery are typical of summer. The NDVI image is color enhanced to represent the relative "greenness" of the surface.

[2]http://www.nssl.noaa.gov/ rabin/vis_wrf

There is also an option to display microphysical quantities from the forecast model as overlays on the visible imagery; vertically integrated cloud liquid water, rain water, ice, snow, and forecast precipitation accumulated in the previous hour. This option is useful to visualize the microphysical composition of cloud fields being viewed, and in relating the model forecast parameters with each other. An example of the available visualizations on a test dataset is shown in Figure 4. The output of the forward radiative transfer model on this NSSL-WRF forecast is shown in Figure 3.

The visible imagery created from the radiative transfer forward model were produced at two different forecast times (18Z and 22Z) for comparison with the neural network version during the NOAA Hazardous Weather Testbed (HWT Clark et al. (2011)) and GOES-R Proving Ground Project in 2010. While the visible imagery from the forward model took hours to compute and were generally available well after the valid time of the forecast, the visible imagery from the neural network approximation were available minutes after the WRF forecasts were produced. It took, on average, 3 minutes of wall-clock time to generate the simulated visible image from a WRF forecast, with nearly 80% of time used in reading the WRF model output. If the approximation is incorporated into the WRF post-processing itself, where the inputs to the neural network are already in main memory, the computation of visible imagery can be reduced to a few seconds per forecast period.

Example images from a 18 hr forecast valid at 18 UTC on Dec 13, 2010 are shown in Figure 5. It should be noted that the simulated visible reflectance is reasonable even though winter-time cases were not part of the training dataset. Arctic air flow over the Great Lakes and south coast U.S. coast was occuring at this time. North to south cloud oriented bands to the south of Lakes Michigan, Huron, and Erie were associated with heavy lake effect snow

squalls. Cloud snow content and surface accumulation are significant in these areas. Several cms of snow were observed near these areas. Parallel cloud bands and cellular clouds off shore of the southeast U.S. and Gulf coasts are evident in the imagery. Given the shallow nature of most of these clouds, they are composed mainly of cloud water without much rainwater. Large areas of thin cloud cover composed mainly of ice surround the snow squalls, and are widespead through an upper-level trough and surface low in the northeast U.S., and with an upper jet stream from northern California to Montana.

Figure 5g shows an observed visible image from the GOES-13 (east) geostationary satellite corresponding to the 18-hour forecast from the NSSL-WRF shown in Figures 5a-f. Much of the difference in cloud locations and visual properties between the observed (Figure 5g) and NN-simulated image (Figure 5a) can be attributed to forecast error. In general the qualitative structure of the cloud areas are similar, especially the deeper (brighter) clouds with precipitation or high water, ice, snow content, and the shallow convective clouds where cold air is moving over the warmer waters off the Atlantic and Gulf of Mexico coasts. Some of the clear sky regions in the observed image (U.S. Midwest) appear bright (high albedo) because of snow cover. The snow covered surface cann't be easily distiguished from cloud cover from the visible image alone. This is not the case in the simulated image since the assumed clear sky albedo is representative of the summer months.

4. Summary

Although a forward radiative transfer model is capable of providing a depiction of non-precipitating clouds in a numerical weather prediction model forecast, present-day forward

models are too slow to run routinely on model forecasts. Therefore, an approximation to the behavior of a radiative transfer model on some representative NWP forecasts was created using a neural network. The resulting approximation is very close to the complex radiative transfer model, but has the advantage of being calculable in a few minutes. This approximation is now carried out routinely in the NOAA Hazardous Weather Testbed and used to visualize NSSL-WRF forecasts.

Acknowledgements

The authors are grateful for support from the NOAA High Performance Computing and Communication (HPCC) program, which made this project possible. Funding for the lead author was provided under NOAA-OU Cooperative Agreement NA17RJ1227.

We would like to thank Justin Sieglaff for his suggestion to include an analysis of the NN approximation error by reflectance value (Figure 2).

REFERENCES

Baum, B., P. Yang, A. Heymsfield, S. Platnick, M. King, Y.-X. Hu, and S. Bedka, 2006: Bulk scattering properties for the remote sensing of ice clouds: Part II. *J. Appl. Meteo.*, **44**, 1896–1911.

Bishop, C., 1995: *Neural Networks for Pattern Recognition*. Oxford.

Clark, A., et al., 2011: An overview of the 2010 Hazardous Weather Testbed Eperimental Forecast Program. *Bull. Amer. Meteo. Soc.*, **subm.**

Dixon, M., Z. Li, H. Lean, N. Roberts, and S. Ballard, 2009: Impact of data assimilation on forecasting convection over the united kingdom using a high-resolution version of the met office unified model. *Mon. Wea. Rev.*, **137**, 1562–1584.

Feltz, W. F., K. M. Bedka, J. A. Otkin, T. Greenwald, and S. A. Ackerman, 2009: Understanding satellite-observed mountain-wave signatures using high-resolution numerical model data. *Wea. Fore.*, **24**, 76–86.

Han, Q., Q. Rossow, R. Welch, A. White, and J. Chou, 1995: Validation of satellite retrievals of cloud microphysics and liquid water path using observations from FIRE. *J. Atmos. Sci.*, **52**, 4183–4195.

Heidinger, A., C. O'Dell, R. Bennartz, and T. Greewald, 2006: The successive order-of-interaction radiative transfer model. part i: Model development. *J. Appl. Meteor. Clim.*, **45**, 1388–1402.

Heymsfield, A., S. Matrosov, and B. Baum, 2003: Ice water path-optical depth relationships for cirrus and deep stratiform ice cloud layers. *J. Appl. Meteor. Clim.*, **42**, 1369–1390.

Hong, S. and J.-O. J. Lim, 2006: The WRF single-moment 6-class microphysics scheme. *J. Korean Meteor. Soc.*, **42**, 129–151.

Jakob, C., 1999: Cloud cover in the ECMWF reanalysis. *J. Climate*, **12**, 947–959.

Janjic, Z. I., 1990: The step-mountain coordinate: physical package. *Mon. Wea. Rev.*, **118**, 1429–1443.

Kain, J. S., S. Dembek, S. J. Weiss, J. L. Case, J. J. Levit, and R. A. Sobash, 2010a: Monitoring selected fields and phenomena every time step. *Weather and Forecasting*, **25**, 1536–1542.

Kain, J. S., et al., 2008: Some practical considerations regarding horizontal resolution in the first generation of operational convection-allowing NWP. *Weather and Forecasting*, **23 (5)**, 931–952.

Kain, J. S., et al., 2010b: Assessing advances in the assimilation of radar data within a collaborative forecasting-research environment. *Weather and Forecasting*, **25**, 1510–1521.

Koch, S. E., B. Ferrier, M. Stolinga, E. Szoke, S. J.Weiss, and J. S. Kain, 2005: The use of simulated radar reflectivity fields in the diagnosis of mesoscale phenomena from high-resolution WRF model forecasts. *12th Conf. on Mesoscale Processes*, Albuquerque, NM, Amer. Meteor. Soc., J4J.7.

Krasnopolsky, V. M., M. Fox-Rabinovitz, H. Tolman, and A. A. Belochitski, 2008: Neural network approach for robust and fast calculation of physical processes in numerical environmental models: Compound parameterization with a quality control of larger errors. *Neural Networks*, **21**, 535–543.

Lakshmanan, V., A. Fritz, T. Smith, K. Hondl, and G. J. Stumpf, 2007: An automated technique to quality control radar reflectivity data. *J. Applied Meteorology*, **46 (3)**, 288–305.

Marzban, C. and G. Stumpf, 1996: A neural network for tornado prediction based on Doppler radar-derived attributes. *J. App. Meteor.*, **35 (5)**, 617–626.

Otkin, J. and T. Greenwald, 2008: Comparison of wrf model-simulated and modis-derived cloud data. *Mon. Wea. Rev.*, **136**, 1957–1970.

Otkin, J., T. Greenwald, J. Sieglaff, and H.-L. Huang, 2009: Validation of a large-scale simulated brightness temperature dataset using SEVIRI satellite observations. *J. Appl. Meteor. Climatol.*, **48**, 1613–1626.

Rogers, E., et al., 2009: The NCEP north american mesoscale modeling system: Recent changes and future plans. *23rd Conf. on Weather Analysis and Forecasting/19th Conf. on Numerical Weather Predicition*, Omaha, NE, Amer. Meteor. Soc., 2A.4.

Sayer, A., G. Thomas, and R. Grainger, 2010: A sea surface reflectance model for AATSR and application to aerosol retrievals. *Atmos. Measurement Tech.*, **44**, 1896–1911.

Skamarock, W., J. Klemp, J. Dudhia, D. Gill, D. Barker, W. Wang, and J. Powers, 2005: A description of the Advanced Research WRF version 2. Tech. Rep. NCAR/TN-468*STR, National Center for Atmospheric Research, 88 pp., Boulder, CO. Available from UCAR Communications, P.O. Box 3000, Boulder CO 80307.

Sundqvist, H., E. Berge, and J. E. Kristjnsson, 1989: Condensation and cloud parameterization studies with a mesoscale numerical weather prediction model. *Mon. Wea. Rev.*, **117**, 1641–1657.

Teixeira, J. and T. Hogan, 2002: Boundary layer clouds in a global atmospheric model:simple cloud cover parameterizations. *J. Climate*, **15**, 1261–1271.

Venkatesan, C., S. Raskar, S. Tambe, B. Kulkarni, and R. Keshavamurty, 1997: Prediction of all india summer monsoon rainfall using error-back-propagation neural networks. *Meteorology and Atmospheric Physics*, **62**, 225–240.

Weisman, M., C. Davis, W. Wang, K. Manning, and J. Klemp, 2008: Experiences with 0-36-h explicit convective forecasts with the WRF-ARW model. *Wea. Forecasting*, **23**, 407–437.

Weiss, S. J., M. E. Pyle, Z. Janjic, D. R. Bright, and G. J. DiMego, 2008: The operational high-resolution window WRF model runs at NCEP: Advantages of multiple model runs for severe convective weather forecasting. *24th Conf. on Severe Local Storms*, Savannah, GA, Amer. Meteor. Soc., P10.8.

List of Figures

5 18-hour forecast valid at 18 UTC on Dec. 13, 2010. Relative values of superimposed quantities (Kg/m**3) increase from blue, to green, to red. (a) Visible image for 18 UTC 13 Dec 2010 simulated using the NN approximation (b) same as a, but with vertically integrated cloud snow content superimposed. (c) same as a, but with 1-hr accumulated precipitation superimposed. (d) same as a, but with vertically integrated cloud ice content superimposed. (e) same as a, but with vertically integrated cloud cloud water content superimposed. (f) same as a, but with vertically integrated cloud rain water content superimposed. (g) Observed GOES-13 visible satellite image 18:15 UTC 13 Dec 2010 26

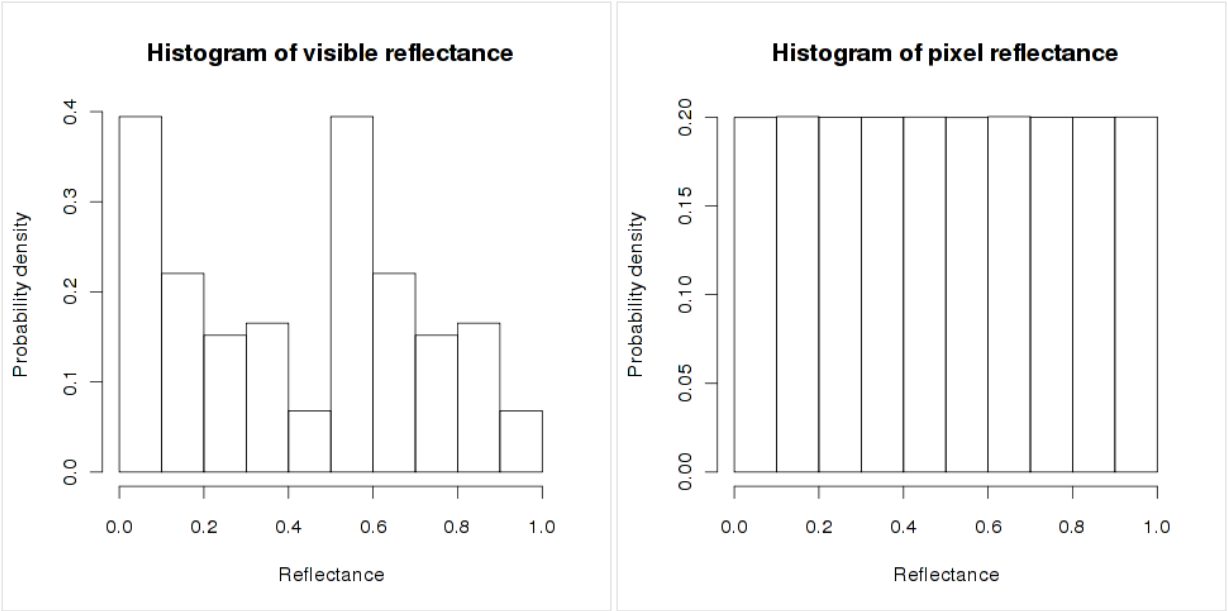

FIG. 1. Effect of histogram equalization. Left: histogram of pixel brightness values based on the NSSL-WRF inputs. Right: histogram of pixel brightness after randomized resampling.

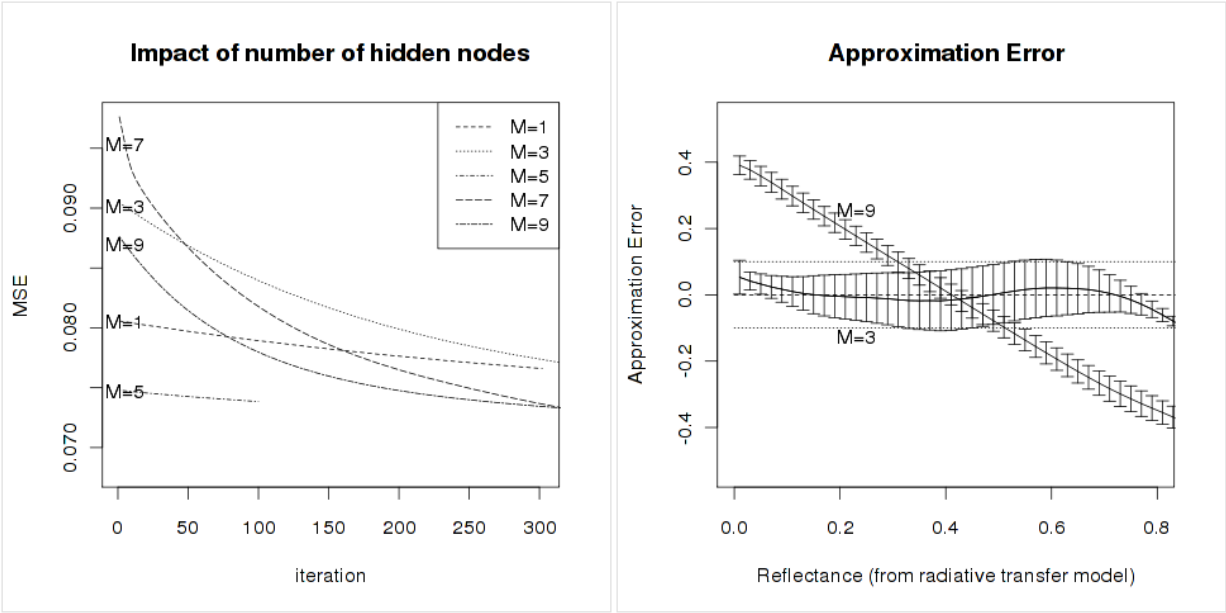

FIG. 2. Effect of the number of hidden nodes (M) on the approximation error. Left: The reduction in mean square error (MSE) during NN training. In general, more hidden nodes lead to lower MSEs. Right: Using 3 hidden nodes has the nice property that the bias is within 0.1 for all reflectances.

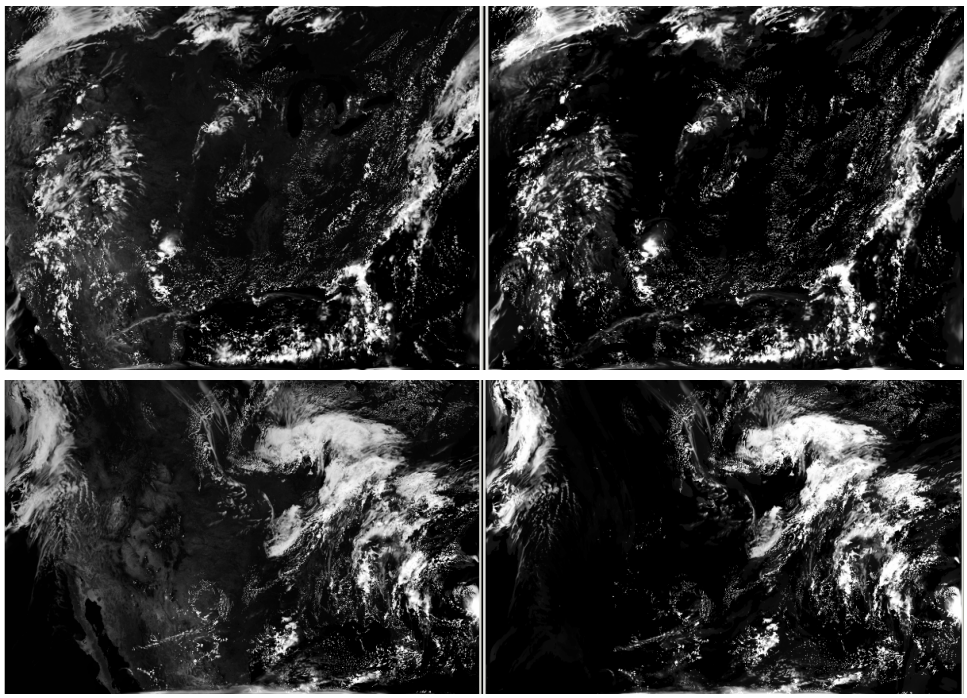

FIG. 3. Top left: Output of forward model run on NSSL-WRF model output valid at 20Z on Aug. 13, 2009 Top right: Output of approximate model run on the same NSSL-WRF model variables. Bottom: same, but on NSSL-WRF forecast valid at 18Z on Aug. 28, 2009.

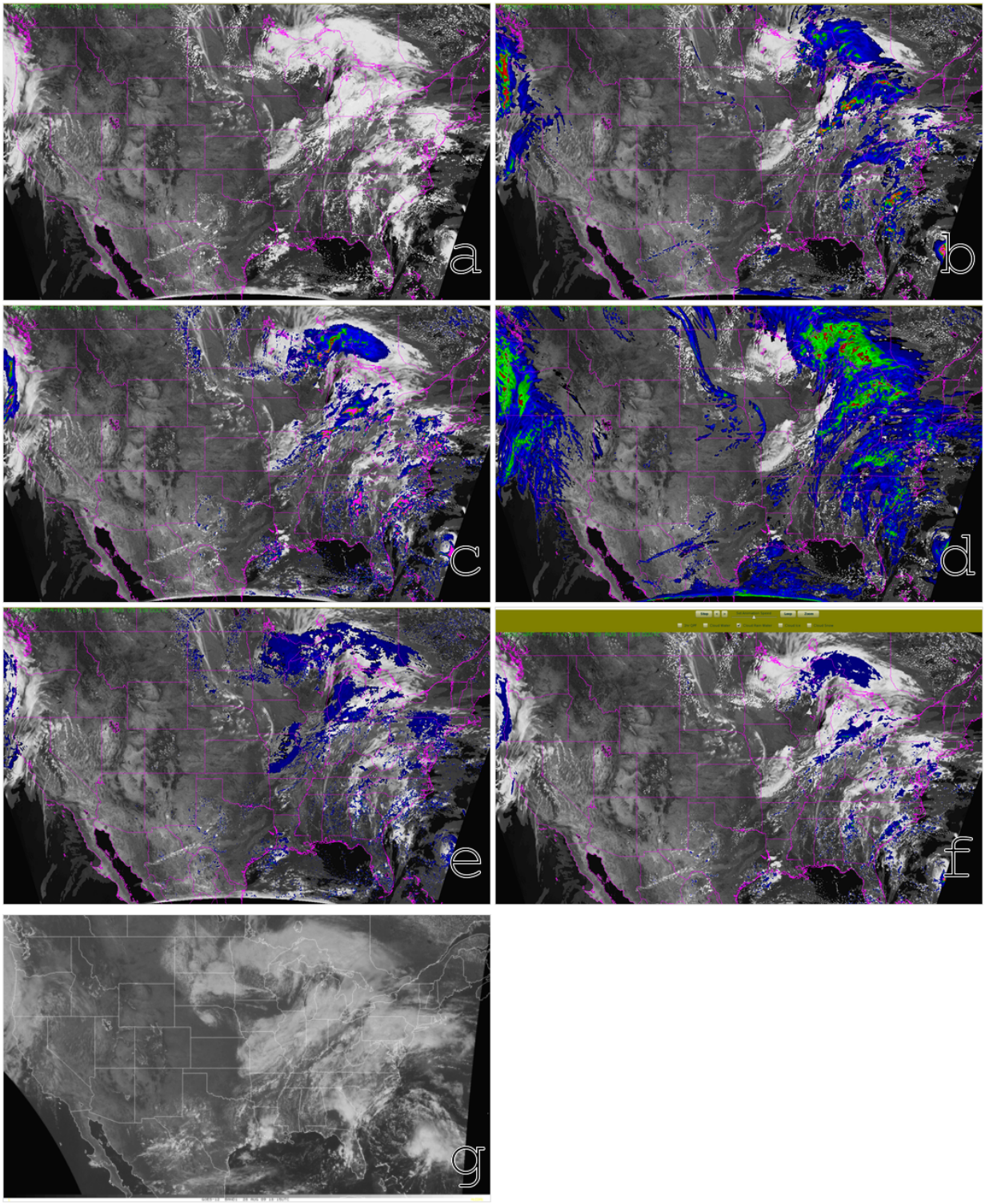

FIG. 4. 18-hour forecast valid at 18 UTC on Aug. 28, 2009. Relative values of superimposed quantities (Kg/m**3) increase from blue, to green, to red. (a) Visible image for 18 UTC 28 Aug 2009 simulated using the NN approximation (b) same as a, but with vertically integrated cloud snow content superimposed. (c) same as a, but with 1-hr accumulated precipitation superimposed. (d) same as a, but with vertically integrated cloud ice content superimposed. (e) same as a, but with vertically integrated cloud cloud water content superimposed. (f) same as a, but with vertically integrated cloud rain water content superimposed. (g) Observed GOES-12 visible satellite image 18:15 UTC 28 Aug 2009

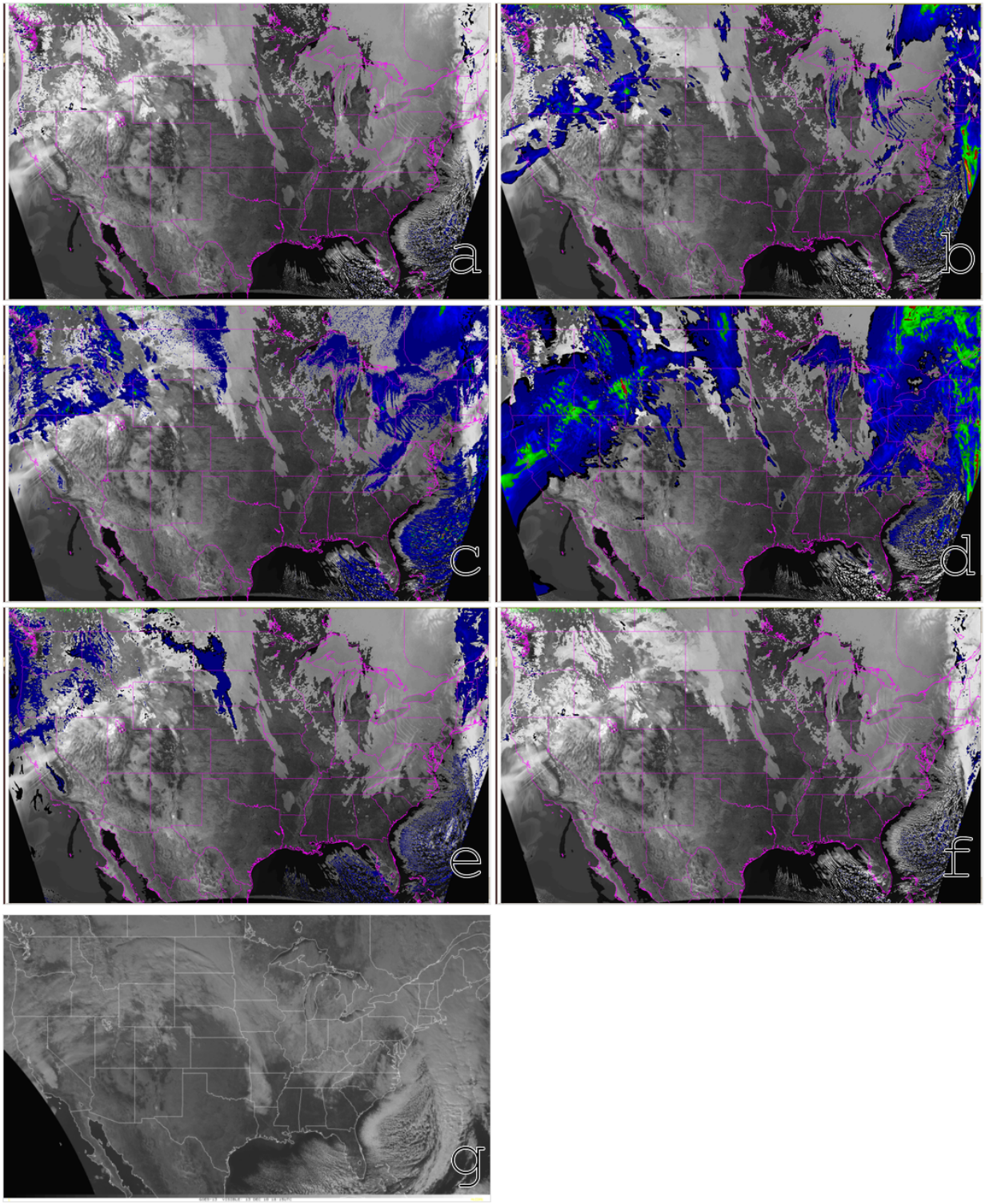

FIG. 5. 18-hour forecast valid at 18 UTC on Dec. 13, 2010. Relative values of superimposed quantities (Kg/m**3) increase from blue, to green, to red. (a) Visible image for 18 UTC 13 Dec 2010 simulated using the NN approximation (b) same as a, but with vertically integrated cloud snow content superimposed. (c) same as a, but with 1-hr accumulated precipitation superimposed. (d) same as a, but with vertically integrated cloud ice content superimposed. (e) same as a, but with vertically integrated cloud cloud water content superimposed. (f) same as a, but with vertically integrated cloud rain water content superimposed. (g) Observed GOES-13 visible satellite image 18:15 UTC 13 Dec 2010